Computers and Mathematics with Applications 66 (2013) 1306–1321

Contents lists available at ScienceDirect

Computers and Mathematics with Applications

journal homepage: www.elsevier.com/locate/camwa

Study of a problem of functionally graded hollow disk under different thermoelasticity theories—An analysis of phase-lag effects

Shweta Kothari *, Santwana Mukhopadhyay

Department of Applied Mathematics, Indian Institute of Technology (BHU), Varanasi 221005, India

ARTICLE INFO

Article history:
Received 10 January 2013
Received in revised form 26 June 2013
Accepted 23 July 2013

Keywords:
Functionally graded material
Type III thermoelasticity
Thermoelasticity with dual phase-lags
Three phase-lag model
Galerkin finite element method

ABSTRACT

The present paper is aimed at the investigation of thermo-mechanical interactions inside a functionally graded hollow disk under different thermoelasticity theories in a unified way. The material of the disk is assumed to be graded along its radial direction such that the profiles of the material properties are assumed to follow a volume-fraction based rule with a power law. The inner and outer surfaces of the disk are subjected to different thermal and mechanical boundary conditions. Galerkin type finite element method is used to solve the coupled equations arising out in the present problem in Laplace transform domain. Solution in space–time domain is obtained by employing a numerical inversion method. A detailed analysis highlighting the effects of phase-lags at different times upon the different fields like displacement, temperature, radial stress and hoop stress for different values of the non-homogeneity index is presented by various graphical plots of our numerical results.

1. Introduction

In the field of heat conduction in deformable bodies, several non-classical theories have been proposed in recent years in order to advocate a theory where the propagation of heat is modeled with a finite speed and thereby removing the so called paradox of infinite speed of propagation for thermoelastic disturbances in the classical "coupled dynamical theory of thermoelasticity", derived by Biot [1]. It should be mentioned here that in addition to the paradox of infinite heat propagation speed, the classical dynamic thermoelasticity theory also suffers from the drawback of either unsatisfactory or poor description of a solid's response at low temperature and to a fast transient effects like short laser pulses. These drawbacks mainly arise due to the fact that this theory is based on Fourier law of heat conduction. The non-classical theories of thermoelasticity are therefore developed with the introduction of modified form of Fourier law. Lord and Shulman [2] proposed an extended thermoelasticity theory (ETE) by incorporating a thermal relaxation time in the Fourier law. The temperature-rate dependent thermoelasticity theory (TRDTE) is later on developed by Green and Lindsay [3] with the introduction of two thermal relaxation parameters in the theory although the Fourier law is kept unchanged in this theory. A completely alternative theoretical development in this subject is made by Green and Naghdi [4–6] which have been the center of active research during the last few decades. In this development Green and Naghdi provided sufficient basic modifications in the constitutive equations and proposed three different models of thermoelasticity, labeled as thermoelasticity of types I, II, and III, that cover a much wider class of heat conduction problems.

Recently, Ozisik and Tzou [7] and Tzou [8] proposed a dual phase-lag (DPL) heat conduction law with the introduction of two delay times. One delay time is caused by the micro-structural interactions (small scale effects of heat transport in space,

* Corresponding author. Tel.: +91 9452047406.
E-mail addresses: skothari.rs.apm@itbhu.ac.in, shweta.kothari5@gmail.com (S. Kothari).

0898-1221/$ – see front matter © 2013 Elsevier Ltd. All rights reserved.
http://dx.doi.org/10.1016/j.camwa.2013.07.029

such as phonon–electron interaction or phonon scattering) and is termed as phase-lag of temperature gradient. Another delay time τ_q is caused due to the fast-transient effects of thermal inertia (or small scale effect of heat transport in time) and called as phase-lag of heat flux. Both the phase lags are small, positive and assumed to be the intrinsic properties of the medium [8]. The recent models of thermoelasticity are thermoelasticity with dual phase-lags (DPLTE) and the thermoelasticity with three phase-lags (TPLTE). The former model is introduced by Chandrasekharaiah [9] by considering the DPL heat conduction law and the other model is given by Roychoudhuri [10] as a generalized version of type III thermoelasticity [5].

Functionally graded materials (FGMs) are composite media that have continuously changing material properties. FGMs are a new branch of materials developed with the purpose of design of structures to withstand suddenly applied loads. The properties of FGMs vary by a gradual change in composition of the constituent materials through the geometry of the structure. This gradual change in material properties of FGMs offers the use of them in abrupt high exposed loads. The smooth variation of properties within FGMs results in lower stress concentration, intensity factors, higher fracture toughness and improved residual stress distribution as compared with traditional laminated composites. Therefore, FGMs have been widely used as thermal shields, wear-resistant linings, heat exchanger tubes, heat engine components and even prostheses (see Birman and Byrd [11] and Bagri and Eslami [12]). In the last decade a great interest is paid to analyze the response of FGMs under different applied mechanical and thermal loads. Tanigawa [13] analyzed the closed-form solutions of problems with the steady-state condition for the heat conduction problems and thermal stresses that occur in a structure made of non-homogeneous materials. Obata and Noda studied steady thermal stresses in a hollow circular cylinder and a hollow sphere of FGMs using the perturbation method [14] and explained the minimization of the thermal stresses. Lutz and Zimmerman reported the analytical solution for the stresses in FG spheres and cylinders [15,16]. Reddy and Chin reported a thermo-mechanical analysis of FG cylinders and plates [17]. Jeon et al. [18] developed an analytical method to tackle thermoelastic problems for a medium with non-homogeneous properties for shear modulus of elasticity, the thermal conductivity and the coefficient of linear thermal expansion. Vel and Betra [19] obtained an exact solution for three-dimensional deformations of a FG rectangular plate subjected to mechanical and thermal loads. Qian and Betra [20] studied transient thermoelastic deformations of a thick FG plate. Ye et al. [21] investigated the axisymmetric thermoelastic problem of a FG transversely isotropic cylindrical shell. El-Naggar et al. [22] studied the radial deformation and the corresponding stresses in a non-homogeneous orthotropic hollow elastic cylinder. An analytical solution for the FG thick spheres under combined steady mechanical and thermal loads is presented by Eslami et al. [23]. Bakhshi et al. [24] studied the response of FG hollow disk based on the classical theory of thermoelasticity under thermal shock loads. Bahtui and Eslami [25,26] investigated the coupled thermoelasticity and generalized coupled thermoelasticity of FG cylindrical shells subjected to a thermal shock load, respectively. Later on, the response of a FG disk is studied by Bagri and Eslami [27] under the ETE theory. Recently, Carrera et al. [28] investigated the effect of thickness stretching in plate/shell structures made by FGM materials. Golmakani and Kadkhodayan [29] studied large deflection analysis of shear deformable FG plates subjected to thermo-mechanical loads. Sun and Luo [30] presented wave propagation and transient response of an infinite FG circular plate under a point impact load. Ezzat and Atef [31] analyzed a problem of generalized magneto–thermoelasticity interactions in a FG viscoelastic layer (Kelvin–Voigt type) due to the presence of thermal shock in the context of the linear theory of generalized thermoelasticity without energy dissipation. For some recent studies upon FGMs in thermoelasticity theories, the Refs. [32–36] and a recent book by Hetnarski and Eslami [37] may also be mentioned.

This article analyzed the thermoelastic interactions inside a FG hollow disk in the context of the recent thermoelasticity theories. The material of the disk is assumed to be graded through its radial direction such that the profiles of all material properties, except the phase-lags, are assumed to follow a volume-fraction based rule with different non-homogeneity indices. The inner surface of the disk is assumed to be traction free with a thermal exposure while the outer surface is fixed and insulated. The governing equations to tackle are obtained in a coupled form. To solve them numerically, Laplace transform technique with Galerkin finite element method is used. To invert the solution in space–time domain a numerical inversion method proposed by Bellman et al. [38] is employed. The effects of non-homogeneity index, phase-lags at different time upon distributions of different physical fields are investigated by various graphical results.

2. Statement of the problem

We consider a functionally graded hollow disk. The functional material properties of FGMs are generally defined by a relation that correlates the effective material properties of FGM to the constituent material properties. Considering a ceramic–metal FGM in which the composition of the metal and ceramic is introduced by a simple law of mixture of material constituents, the effective material properties of FGM may be defined as

$$P = V_m\,(P_m - P_c) + P_c, \tag{1}$$

where V_m is the volume fraction of the metal, P is the effective property of FGM and the subscripts m and c indicate the metal and ceramic features, respectively. Therefore, P_m and P_c are the properties of metal and ceramic, respectively.

3. Basic governing equations

The governing equations in usual indicial notation for isotropic FGMs in the absence of heat sources and body forces are considered as follows:

Equations of motion:

$$\sigma_{ij,j} = \rho \ddot{u}_i. \tag{2}$$

Energy balance equation:

$$q_{i,i} = -T_0 \dot{S}. \tag{3}$$

Entropy equation:

$$S = \frac{\rho c}{T_0}\theta + \beta \delta_{ij} e_{ij}. \tag{4}$$

Stress–strain–temperature relation:

$$\sigma_{ij} = 2\mu e_{ij} + (\lambda e_{kk} - \beta\theta)\,\delta_{ij}. \tag{5}$$

Strain–displacement relation:

$$2e_{ij} = u_{i,j} + u_{j,i}. \tag{6}$$

Law of heat conduction in the context of thermoelasticity theory of type III (GN-III) [5]:

$$\dot{q}_i = -\left(K^* + K\frac{\partial}{\partial t}\right)\theta_{,i}. \tag{7}$$

Law of heat conduction under dual phase-lag theory (DPLTE) [8]:

$$\left(1 + \tau_q \frac{\partial}{\partial t} + \frac{\tau_q^2}{2}\frac{\partial^2}{\partial t^2}\right) q_i = -K\left(1 + \tau_T \frac{\partial}{\partial t}\right)\theta_{,i}. \tag{8}$$

Law of heat conduction based on three phase-lag theory (TPLTE) [10]:

$$\left(1 + \tau_q \frac{\partial}{\partial t} + \frac{\tau_q^2}{2}\frac{\partial^2}{\partial t^2}\right) q_i = -\left[K^*\left(1 + \tau_v \frac{\partial}{\partial t}\right) + K\frac{\partial}{\partial t}\left(1 + \tau_T \frac{\partial}{\partial t}\right)\right]\theta_{,i}. \tag{9}$$

In the above equations u_i, σ_{ij}, e_{ij} and q_i are the components of displacement vector, stress tensor, strain tensor and heat flux vector, respectively. $\theta = T - T_0$, where T is the absolute temperature and T_0 is the reference temperature of the medium in its natural state. S represents entropy per unit volume. ρ is the mass density and c is the specific heat per unit mass. K is the thermal conductivity and K^* is the rate of thermal conductivity. λ, μ are Lamè's elastic constants and β is the thermoelastic material constant given by $\beta = (3\lambda + 2\mu)\alpha_t$ where α_t is the coefficient of linear thermal expansion. τ_q, τ_T and τ_v are the phase-lags due to the heat flux, temperature gradient and the thermal displacement gradient, respectively. A superposed dot denotes partial differentiation with respect to time t and δ_{ij} is the Kronecker's delta.

From Eqs. (2), (5) and (6), we can obtain the coupled equations of motion in terms of displacement and temperature as

$$\left(\lambda u_{k,k}\delta_{ij} + \mu\left(u_{i,j} + u_{j,i}\right) - \beta\theta\delta_{ij}\right)_{,j} = \rho\ddot{u}_i. \tag{10}$$

Heat conduction equation under GN-III is obtained from Eqs. (3), (4) and (7) as

$$\left[K^*\theta_{,i} + K\frac{\partial}{\partial t}\theta_{,i}\right]_{,i} = \frac{\partial}{\partial t}\left(\rho c\frac{\partial\theta}{\partial t} + \beta T_0 \frac{\partial u_{i,i}}{\partial t}\right). \tag{11}$$

Using (3), (4) and (8), the heat conduction equation under DPLTE is given by

$$\left[K\left(1 + \tau_T\frac{\partial}{\partial t}\right)\theta_{,i}\right]_{,i} = \left(1 + \tau_q\frac{\partial}{\partial t} + \frac{\tau_q^2}{2}\frac{\partial^2}{\partial t^2}\right)\left(\rho c\frac{\partial\theta}{\partial t} + \beta T_0\frac{\partial u_{i,i}}{\partial t}\right). \tag{12}$$

Heat conduction equation under TPLTE is obtained from (3), (4) and (9) as

$$\left[K^*\left(1 + \tau_v\frac{\partial}{\partial t}\right)\theta_{,i} + K\frac{\partial}{\partial t}\left(1 + \tau_T\frac{\partial}{\partial t}\right)\theta_{,i}\right]_{,i} = \left(1 + \tau_q\frac{\partial}{\partial t} + \frac{\tau_q^2}{2}\frac{\partial^2}{\partial t^2}\right)\frac{\partial}{\partial t}\left(\rho c\frac{\partial\theta}{\partial t} + \beta T_0\frac{\partial u_{i,i}}{\partial t}\right). \tag{13}$$

The material properties, except the phase-lags, which appeared in the preceding equations (2)–(13) for the FGMs are the effective material properties and are position dependent functions.

4. Problem formulation

In the present problem, we consider a hollow disk with inner and outer radius r_{in} and r_{out}, respectively, initially at rest and reference temperature T_0, under axis-symmetric thermal shock load applied into its inner boundary. The generalized coupled thermoelastic equations of the disk, with plane stress assumption, based on the above discussed thermoelasticity theories are obtained from Eqs. (5) and (10)–(13) as

$$\sigma_{rr} = 2\mu\frac{\partial u}{\partial r} + \bar{\lambda}\left(\frac{\partial u}{\partial r} + \frac{u}{r}\right) - \bar{\beta}\theta \tag{14}$$

$$\sigma_{\theta\theta} = 2\mu\frac{u}{r} + \bar{\lambda}\left(\frac{\partial u}{\partial r} + \frac{u}{r}\right) - \bar{\beta}\theta \tag{15}$$

$$\left(\bar{\lambda}+2\mu\right)\left[\frac{\partial^2 u}{\partial r^2} + \frac{1}{r}\frac{\partial u}{\partial r} - \frac{u}{r^2}\right] + \frac{\partial u}{\partial r}\frac{\partial\left(\bar{\lambda}+2\mu\right)}{\partial r} + \frac{u}{r}\frac{\partial\bar{\lambda}}{\partial r} - \left[\bar{\beta}\frac{\partial\theta}{\partial r} + \theta\frac{\partial\bar{\beta}}{\partial r}\right] = \rho\frac{\partial^2 u}{\partial t^2} \tag{16}$$

$$\frac{1}{r}\left(K^* + K\frac{\partial}{\partial t}\right)\frac{\partial\theta}{\partial r} + \left(\frac{\partial K^*}{\partial r} + \frac{\partial K}{\partial r}\frac{\partial}{\partial t}\right)\frac{\partial\theta}{\partial r} + \left(K^* + K\frac{\partial}{\partial t}\right)\frac{\partial^2\theta}{\partial r^2} = \frac{\partial}{\partial t}\left(\rho c\frac{\partial\theta}{\partial t} + \bar{\beta}T_0\frac{\partial}{\partial t}\left(\frac{\partial u}{\partial r} + \frac{u}{r}\right)\right) \tag{17}$$

$$\left(1+\tau_T\frac{\partial}{\partial t}\right)\left[\left\{\frac{\partial^2\theta}{\partial r^2} + \frac{1}{r}\frac{\partial\theta}{\partial r}\right\}K + \frac{\partial\theta}{\partial r}\frac{\partial K}{\partial r}\right] - \left(1+\tau_q\frac{\partial}{\partial t} + \frac{\tau_q^2}{2}\frac{\partial^2}{\partial t^2}\right)\rho c\frac{\partial\theta}{\partial t}$$
$$- \left(1+\tau_q\frac{\partial}{\partial t} + \frac{\tau_q^2}{2}\frac{\partial^2}{\partial t^2}\right)\bar{\beta}T_0\frac{\partial}{\partial t}\left(\frac{\partial u}{\partial r} + \frac{u}{r}\right) = 0 \tag{18}$$

$$\left[\left(1+\tau_v\frac{\partial}{\partial t}\right)K^* + \left(1+\tau_T\frac{\partial}{\partial t}\right)K\frac{\partial}{\partial t}\right]\left(\frac{\partial^2\theta}{\partial r^2} + \frac{1}{r}\frac{\partial\theta}{\partial r}\right) + \left[\left(1+\tau_v\frac{\partial}{\partial t}\right)\frac{\partial K^*}{\partial r} + \left(1+\tau_T\frac{\partial}{\partial t}\right)\frac{\partial K}{\partial r}\frac{\partial}{\partial t}\right]\frac{\partial\theta}{\partial r}$$
$$= \left(1+\tau_q\frac{\partial}{\partial t} + \frac{\tau_q^2}{2}\frac{\partial^2}{\partial t^2}\right)\frac{\partial}{\partial t}\left(\rho c\frac{\partial\theta}{\partial t} + \bar{\beta}T_0\frac{\partial}{\partial t}\left(\frac{\partial u}{\partial r} + \frac{u}{r}\right)\right) \tag{19}$$

where $\bar{\lambda} = \frac{2\mu}{\lambda+2\mu}\lambda$ and $\bar{\beta} = \frac{2\mu}{\lambda+2\mu}\beta$ due to the assumption of plane stress condition.

Now, we consider that the inner surface and outer surface of the disk are made of ceramic and metal, respectively and the gradual change in composition of the constituent materials in the radial direction is assumed to vary in the form as

$$V_m = \left(\frac{r - r_{in}}{r_{out} - r_{in}}\right)^n$$

where r is the radial coordinate and n is the non-homogeneity index that govern the distribution of the constituent materials through the geometry of the disk. Fig. 1 shows the distribution of the material composition in the functionally graded hollow disk along the radial direction. The non-homogeneity index, n may be varied to obtain different profiles for the distribution of constituent materials. When $n \to 0$ the effective properties of hollow disk are followed by metal and when $n \to \infty$ they are followed by ceramic.

For simplicity of the problem, we introduce the following non-dimensional variables and notations:

$$\left.\begin{aligned} &r' = c_1\eta_0 r, \quad \theta' = \frac{\theta}{T_d}, \quad t' = c_1^2\eta_0 t, \quad \tau_q' = c_1^2\eta_0\tau_q, \quad \tau_T' = c_1^2\eta_0\tau_T, \quad \tau_v' = c_1^2\eta_0\tau_v \\ &u' = \frac{c_1\eta_0\left(\bar{\lambda}_m + 2\mu_m\right)}{\bar{\beta}_m T_d}u, \quad \sigma_{ij}' = \frac{\sigma_{ij}}{\bar{\beta}_m T_d}, \quad c_1^2 = \frac{\left(\bar{\lambda}_m + 2\mu_m\right)}{\rho_m}, \quad \eta_0 = \frac{\rho_m c_m}{K_m} \end{aligned}\right\} \tag{20}$$

where T_d is a dimensionless characteristic temperature.

By using above dimensionless quantities and dropping the prime notation for sake of convenience, Eqs. (14)–(19) reduce to the form

$$\sigma_{rr} = \frac{2\mu}{\bar{\lambda}_m + 2\mu_m}\frac{\partial u}{\partial r} + \frac{\bar{\lambda}}{\bar{\lambda}_m + 2\mu_m}\left(\frac{\partial u}{\partial r} + \frac{u}{r}\right) - \frac{\bar{\beta}}{\bar{\beta}_m}\theta \tag{21}$$

$$\sigma_{\theta\theta} = \frac{2\mu}{\bar{\lambda}_m + 2\mu_m}\frac{u}{r} + \frac{\bar{\lambda}}{\bar{\lambda}_m + 2\mu_m}\left(\frac{\partial u}{\partial r} + \frac{u}{r}\right) - \frac{\bar{\beta}}{\bar{\beta}_m}\theta \tag{22}$$

$$\left(\bar{\lambda}+2\mu\right)\left[\frac{\partial^2 u}{\partial r^2} + \frac{1}{r}\frac{\partial u}{\partial r} - \frac{u}{r^2}\right] + \frac{\partial u}{\partial r}\frac{\partial\left(\bar{\lambda}+2\mu\right)}{\partial r} + \frac{u}{r}\frac{\partial\bar{\lambda}}{\partial r} - \rho c_1^2\frac{\partial^2 u}{\partial t^2} - \frac{\left(\bar{\lambda}_m + 2\mu_m\right)}{\bar{\beta}_m}\left[\bar{\beta}\frac{\partial\theta}{\partial r} + \theta\frac{\partial\bar{\beta}}{\partial r}\right] = 0 \tag{23}$$

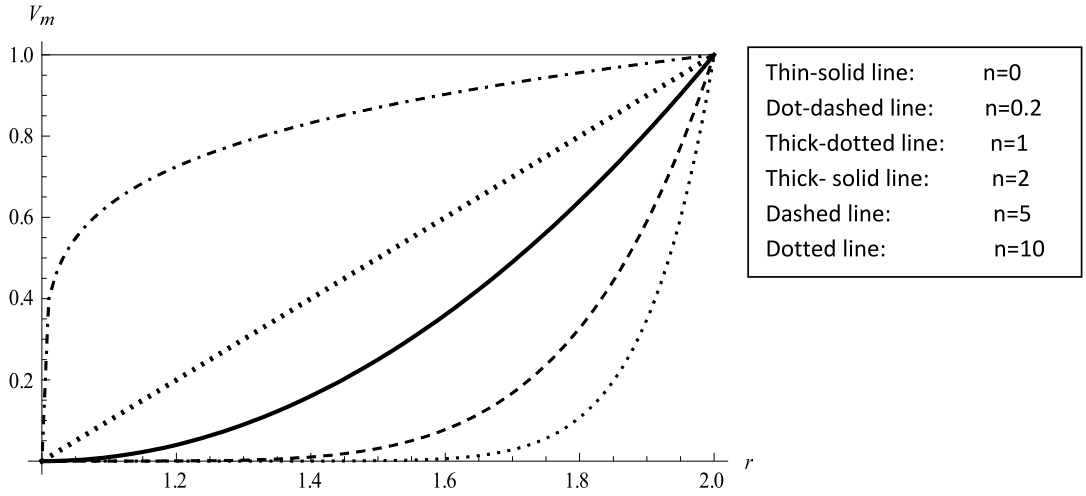

Fig. 1. Distribution of metal volume fraction with $r_{in} = 1$ and $r_{out} = 2$.

$$\left(\frac{K^*}{a_0}+\frac{K}{K_m}\frac{\partial}{\partial t}\right)\left\{\frac{\partial^2\theta}{\partial r^2}+\frac{1}{r}\frac{\partial\theta}{\partial r}\right\}+\left(\frac{1}{a_0}\frac{\partial K^*}{\partial r}+\frac{1}{K_m}\frac{\partial K}{\partial r}\frac{\partial}{\partial t}\right)\frac{\partial\theta}{\partial r}=\frac{\partial}{\partial t}\left(\frac{\rho c}{\rho_m c_m}\frac{\partial\theta}{\partial t}+\varepsilon\frac{\bar\beta}{\bar\beta_m}\frac{\partial}{\partial t}\left(\frac{\partial u}{\partial r}+\frac{u}{r}\right)\right) \tag{24}$$

$$\left(1+\tau_T\frac{\partial}{\partial t}\right)\left[\left\{\frac{\partial^2\theta}{\partial r^2}+\frac{1}{r}\frac{\partial\theta}{\partial r}\right\}\frac{K}{K_m}+\frac{1}{K_m}\frac{\partial\theta}{\partial r}\frac{\partial K}{\partial r}\right]-\left(1+\tau_q\frac{\partial}{\partial t}+\frac{\tau_q^2}{2}\frac{\partial^2}{\partial t^2}\right)\frac{\rho c}{\rho_m c_m}\frac{\partial\theta}{\partial t}$$
$$-\varepsilon\left(1+\tau_q\frac{\partial}{\partial t}+\frac{\tau_q^2}{2}\frac{\partial^2}{\partial t^2}\right)\frac{\bar\beta}{\bar\beta_m}\frac{\partial}{\partial t}\left(\frac{\partial u}{\partial r}+\frac{u}{r}\right)=0 \tag{25}$$

$$\left(\frac{K^*}{a_0}\left(1+\tau_v\frac{\partial}{\partial t}\right)+\frac{K}{K_m}\left(1+\tau_T\frac{\partial}{\partial t}\right)\frac{\partial}{\partial t}\right)\left\{\frac{\partial^2\theta}{\partial r^2}+\frac{1}{r}\frac{\partial\theta}{\partial r}\right\}$$
$$+\left(\frac{1}{a_0}\frac{\partial K^*}{\partial r}\left(1+\tau_v\frac{\partial}{\partial t}\right)+\frac{1}{K_m}\frac{\partial K}{\partial r}\left(1+\tau_T\frac{\partial}{\partial t}\right)\frac{\partial}{\partial t}\right)\frac{\partial\theta}{\partial r}$$
$$=\left(1+\tau_q\frac{\partial}{\partial t}+\frac{\tau_q^2}{2}\frac{\partial^2}{\partial t^2}\right)\frac{\partial}{\partial t}\left(\frac{\rho c}{\rho_m c_m}\frac{\partial\theta}{\partial t}+\varepsilon\frac{\bar\beta}{\bar\beta_m}\frac{\partial}{\partial t}\left(\frac{\partial u}{\partial r}+\frac{u}{r}\right)\right) \tag{26}$$

where $\varepsilon=\frac{\bar\beta_m^2 T_0}{(\bar\lambda_m+2\mu_m)\rho_m c_m}$ and $a_0=c_1^2\eta_0 K_m$.

The dimensionless heat conduction equations given by (24)–(26) can now be written in a unified form as

$$\left(1+\tau_v\frac{\partial}{\partial t}\right)\left(\frac{K^*}{a_0}\left\{\frac{\partial^2\theta}{\partial r^2}+\frac{1}{r}\frac{\partial\theta}{\partial r}\right\}+\frac{1}{a_0}\frac{\partial K^*}{\partial r}\frac{\partial\theta}{\partial r}\right)$$
$$+\left(\delta_{2z}+\delta_{1z}\frac{\partial}{\partial t}\right)\left[\left(1+\tau_T\frac{\partial}{\partial t}\right)\left(\frac{K}{K_m}\left\{\frac{\partial^2\theta}{\partial r^2}+\frac{1}{r}\frac{\partial\theta}{\partial r}\right\}+\frac{1}{K_m}\frac{\partial K}{\partial r}\frac{\partial\theta}{\partial r}\right)-\frac{\rho c}{\rho_m c_m}\left(1+\tau_q\frac{\partial}{\partial t}+\frac{\tau_q^2}{2}\frac{\partial^2}{\partial t^2}\right)\frac{\partial\theta}{\partial t}\right]$$
$$-\left(\delta_{2z}+\delta_{1z}\frac{\partial}{\partial t}\right)\left(1+\tau_q\frac{\partial}{\partial t}+\frac{\tau_q^2}{2}\frac{\partial^2}{\partial t^2}\right)\varepsilon\frac{\bar\beta}{\bar\beta_m}\frac{\partial}{\partial t}\left(\frac{\partial u}{\partial r}+\frac{u}{r}\right)=0. \tag{27}$$

We can obtain each heat conduction equation by setting different values of phase-lags and the values of z in Kronecker delta δ_{iz}, $(i = 1,\ 2)$ as follows:

I. thermoelasticity of type GN-III: $z = 1$, $\tau_v = \tau_T = \tau_q = 0$, $K^* > 0$;
II. thermoelasticity with one relaxation time (ETE): $z = 2$, $\tau_v = 0$, $\tau_T = 0$, $\tau_q > 0$, $\tau_q^2 = 0$, $K^* = 0$;
III. thermoelasticity with dual phase-lags (DPLTE): $z = 2$, $\tau_v = 0$, $\tau_T > 0$, $\tau_q > 0$, $2\tau_T > \tau_q$, $K^* = 0$;
IV. thermoelasticity with three phase-lags (TPLTE): $z = 1$, $\tau_v > 0$, $\tau_T > 0$, $\tau_q > 0$, $\tau_q > \tau_T > \tau_v$, $K^* > 0$.

Therefore, we can now study the coupled field equations of GN-III, ETE, DPLTE and TPLTE simultaneously by considering Eqs. (23) and (27) for displacement and temperature.

In order to define the boundary conditions at the inner and outer surfaces, the inner surface is assumed to be traction free but exposed to a thermal shock while the outer surface is fixed and thermally insulated. Thus the mechanical and thermal boundary conditions at the inner and outer surfaces of the disk are defined as

$$\begin{aligned} &\theta = 1 - e^{-10000t}, \qquad \sigma_{rr} = 0, \quad \text{at } r = a \\ &\frac{\partial \theta}{\partial r} = 0, \qquad u = 0, \quad \text{at } r = b \end{aligned} \tag{28}$$

where t is the dimensionless time a and b are the dimensionless inner and outer radii, respectively.

5. Solution by using Laplace transforms technique and Galerkin finite element method

The Eqs. (23) and (27) are coupled differential equations. The general closed form solution for the present problem is therefore a formidable task. A suitable transfinite element method [27] via Laplace transform technique is therefore employed here to find the solution of the displacement and temperature field in the space domain. Finally, the temperature, displacement and stresses in the physical domain can be obtained by applying a suitable numerical method of Laplace inversion.

The Laplace transform of any function $f(t)$ is defined as

$$\bar{f}(s) = \int_0^\infty e^{-st} f(t)\, dt, \quad s > 0$$

where s is the Laplace transform parameter.

Therefore, applying Laplace transform to Eqs. (21)–(23) and (27) and using homogeneous initial conditions, we obtain

$$\bar{\sigma}_{rr} = \frac{2\mu}{\bar{\lambda}_m + 2\mu_m}\frac{\partial \bar{u}}{\partial r} + \frac{\bar{\lambda}}{\bar{\lambda}_m + 2\mu_m}\left(\frac{\partial \bar{u}}{\partial r} + \frac{\bar{u}}{r}\right) - \frac{\bar{\beta}}{\bar{\beta}_m}\bar{\theta} \tag{29}$$

$$\bar{\sigma}_{\theta\theta} = \frac{2\mu}{\bar{\lambda}_m + 2\mu_m}\frac{\bar{u}}{r} + \frac{\bar{\lambda}}{\bar{\lambda}_m + 2\mu_m}\left(\frac{\partial \bar{u}}{\partial r} + \frac{\bar{u}}{r}\right) - \frac{\bar{\beta}}{\bar{\beta}_m}\bar{\theta} \tag{30}$$

$$\left(\bar{\lambda} + 2\mu\right)\left[\frac{\partial^2 \bar{u}}{\partial r^2} + \frac{1}{r}\frac{\partial \bar{u}}{\partial r} - \frac{\bar{u}}{r^2}\right] + \frac{\partial \bar{u}}{\partial r}\frac{\partial\left(\bar{\lambda} + 2\mu\right)}{\partial r} + \frac{\bar{u}}{r}\frac{\partial \bar{\lambda}}{\partial r} - \rho c_1^2 s^2 \bar{u} - \frac{\left(\bar{\lambda}_m + 2\mu_m\right)}{\bar{\beta}_m}\left[\bar{\beta}\frac{\partial \bar{\theta}}{\partial r} + \bar{\theta}\frac{\partial \bar{\beta}}{\partial r}\right] = 0 \tag{31}$$

$$\begin{aligned} &(1 + \tau_\nu s)\left(\frac{K^*}{a_0}\left\{\frac{\partial^2 \bar{\theta}}{\partial r^2} + \frac{1}{r}\frac{\partial \bar{\theta}}{\partial r}\right\} + \frac{1}{a_0}\frac{\partial K^*}{\partial r}\frac{\partial \bar{\theta}}{\partial r}\right) \\ &\quad + (\delta_{2z} + \delta_{1z} s)\left[(1 + \tau_T s)\left(\frac{K}{K_m}\left\{\frac{\partial^2 \bar{\theta}}{\partial r^2} + \frac{1}{r}\frac{\partial \bar{\theta}}{\partial r}\right\} + \frac{1}{K_m}\frac{\partial K}{\partial r}\frac{\partial \bar{\theta}}{\partial r}\right) - \frac{\rho c s}{\rho_m c_m}\left(1 + \tau_q s + \frac{\tau_q^2}{2}s^2\right)\bar{\theta}\right] \\ &\quad - (\delta_{2z} + \delta_{1z} s)\left(1 + \tau_q s + \frac{\tau_q^2}{2}s^2\right)\varepsilon\frac{\bar{\beta}}{\bar{\beta}_m} s\left(\frac{\partial \bar{u}}{\partial r} + \frac{\bar{u}}{r}\right) = 0. \end{aligned} \tag{32}$$

Also the Laplace transform of the boundary conditions given by (28) yields

$$\begin{aligned} &\bar{\theta} = 10000/(s^2 + 10000s) \qquad \bar{\sigma}_{rr} = 0 \quad \text{at } r = a \\ &\frac{\partial \bar{\theta}}{\partial r} = 0 \qquad \bar{u} = 0 \quad \text{at } r = b. \end{aligned} \tag{33}$$

Now, we employ finite element method to solve the coupled equations (31) and (32). For this, the geometry of the disk is divided into some discrete elements along the radius of the disk. Considering the base element (e), the displacement and temperature fields over the base element are approximated as

$$\bar{u}^{(e)} = \sum_{i=1}^{l} N_i \bar{U}_i \quad \text{and} \quad \bar{\theta}^{(e)} = \sum_{i=1}^{l} N_i \bar{\theta}_i \tag{34}$$

where the N_i denotes the shape function that approximates the displacement and temperature fields in the base element and l is the number of nodes in the base element. $\bar{U}_i$ and $\bar{\theta}_i$ are therefore the nodal values of displacement and temperature, respectively.

Employing the approximated fields for the displacement and temperature in the base element (e) and applying the Galerkin finite element method over the volume of the base element $V^{(e)}$, Eqs. (31) and (32) become

$$\int_{V^{(e)}} \left[\left\{ \left(\bar{\lambda}+2\mu\right)\left[\frac{\partial^2}{\partial r^2}+\frac{1}{r}\frac{\partial}{\partial r}-\frac{1}{r^2}\right]+\frac{\partial\left(\bar{\lambda}+2\mu\right)}{\partial r}\frac{\partial}{\partial r}+\frac{1}{r}\frac{\partial\bar{\lambda}}{\partial r}-\rho c_1^2 s^2\right\}\bar{u}^{(e)} - \frac{\left(\bar{\lambda}_m+2\mu_m\right)}{\bar{\beta}_m}\left[\bar{\beta}\frac{\partial}{\partial r}+\frac{\partial\bar{\beta}}{\partial r}\right]\bar{\theta}^{(e)}\right] N_i dv = 0 \tag{35}$$

$$\int_{V^{(e)}} \left[\left\{ (1+\tau_v s)\left(\frac{K^*}{a_0}\left\{\frac{\partial^2}{\partial r^2}+\frac{1}{r}\frac{\partial}{\partial r}\right\}+\frac{1}{a_0}\frac{\partial K^*}{\partial r}\frac{\partial}{\partial r}\right) + (\delta_{2z}+\delta_{1z}s)\left[(1+\tau_T s)\left(\frac{K}{K_m}\left\{\frac{\partial^2}{\partial r^2}+\frac{1}{r}\frac{\partial}{\partial r}\right\}+\frac{1}{K_m}\frac{\partial K}{\partial r}\frac{\partial}{\partial r}\right)-\frac{\rho cs}{\rho_m c_m}\left(1+\tau_q s+\frac{\tau_q^2}{2}s^2\right)\right]\right\}\bar{\theta}^{(e)} - (\delta_{2z}+\delta_{1z}s)\left(1+\tau_q s+\frac{\tau_q^2}{2}s^2\right)\varepsilon\frac{\bar{\beta}}{\bar{\beta}_m}s\left(\frac{\partial}{\partial r}+\frac{1}{r}\right)\bar{u}^{(e)}\right] N_i\, dv = 0 \tag{36}$$

where $i = 1, 2, \ldots, l$.

Now, the weak formulation is applied to the terms involving the derivatives of the second order to lower their orders and to extract mixed boundary conditions with respect to the radial variable. Using the local coordinates $\eta = r - r_i$, where r_i is the radius of the first node of the base element in radial direction, Eqs. (35) and (36) reduce to the following equations:

$$\int_0^L \left[-\left[\left\{-\frac{\left(\bar{\lambda}+2\mu\right)}{(\eta+r_i)^2}+\frac{1}{\eta+r_i}\frac{\partial\bar{\lambda}}{\partial\eta}-\rho c_1^2 s^2\right\}\bar{u}^{(e)}-\frac{\left(\bar{\lambda}_m+2\mu_m\right)}{\bar{\beta}_m}\left[\bar{\beta}\frac{\partial}{\partial\eta}+\frac{\partial\bar{\beta}}{\partial\eta}\right]\bar{\theta}^{(e)}\right] N_i\,(\eta+r_i) + \left(\bar{\lambda}+2\mu\right)(\eta+r_i)\frac{\partial N_i}{\partial\eta}\frac{\partial\bar{u}^{(e)}}{\partial\eta}\right] d\eta = \left(\bar{\lambda}+2\mu\right)(\eta+r_i)\,N_i\frac{\partial\bar{u}^{(e)}}{\partial\eta}\Big|_0^L \tag{37}$$

$$\int_0^L \left[(\delta_{2z}+\delta_{1z}s)\left(1+\tau_q s+\frac{\tau_q^2}{2}s^2\right)\left[\frac{\rho cs}{\rho_m c_m}\bar{\theta}^{(e)}+\frac{\varepsilon\bar{\beta}}{\bar{\beta}_m}s\left(\frac{\partial}{\partial\eta}+\frac{1}{\eta+r_i}\right)\bar{u}^{(e)}\right] N_i\,(\eta+r_i) + (1+\tau_v s)\frac{K^*}{a_0}\frac{\partial N_i}{\partial\eta}\,(\eta+r_i)\frac{\partial\bar{\theta}^{(e)}}{\partial\eta}+(\delta_{2z}+\delta_{1z}s)(1+\tau_T s)\frac{K}{K_m}\frac{\partial N_i}{\partial\eta}\,(\eta+r_i)\frac{\partial\bar{\theta}^{(e)}}{\partial\eta}\right] d\eta = (1+\tau_v s)\frac{K^*}{a_0}N_i\,(\eta+r_i)\frac{\partial\bar{\theta}^{(e)}}{\partial\eta}\Big|_0^L + (\delta_{2z}+\delta_{1z}s)(1+\tau_T s)\frac{K}{K_m}N_i\,(\eta+r_i)\frac{\partial\bar{\theta}^{(e)}}{\partial\eta}\Big|_0^L \tag{38}$$

where L is the length of the base element (e) along the radius.

Therefore, substituting from Eq. (34) into Eqs. (37) and (38), the transfinite element formulation in matrix form is obtained as

$$\begin{bmatrix}[K_{11}] & [K_{12}]\\ [K_{21}] & [K_{22}]\end{bmatrix}\begin{Bmatrix}\{\bar{U}^{(e)}\}\\ \{\bar{\theta}^{(e)}\}\end{Bmatrix} = \begin{Bmatrix}\{F^{(e)}\}\\ \{Q^{(e)}\}\end{Bmatrix} \tag{39}$$

where the sub matrices $[K_{11}]$, $[K_{12}]$, $[K_{21}]$, $[K_{22}]$, $\{F^{(e)}\}$ and $\{Q^{(e)}\}$ for the base element (e) are obtained as

$$\left[K_{11}^{ij}\right] = \int_0^L \left[\left(\bar{\lambda}+2\mu\right)\frac{1}{(\eta+r_i)}N_iN_j - N_iN_j\frac{\partial\bar{\lambda}}{\partial\eta}+\rho c_1^2 s^2 N_iN_j\,(\eta+r_i)+\left(\bar{\lambda}+2\mu\right)(\eta+r_i)\frac{\partial N_i}{\partial\eta}\frac{\partial N_j}{\partial\eta}\right] d\eta \tag{40}$$

$$\left[K_{12}^{ij}\right] = \frac{\left(\bar{\lambda}_m+2\mu_m\right)}{\bar{\beta}_m}\int_0^L N_i\,(\eta+r_i)\left[\bar{\beta}\frac{\partial N_j}{\partial\eta}+N_j\frac{\partial\bar{\beta}}{\partial\eta}\right] d\eta \tag{41}$$

$$\left[K_{21}^{ij}\right] = \frac{\varepsilon s}{\bar{\beta}_m}\left(1+\tau_q s+\frac{\tau_q^2}{2}s^2\right)(\delta_{2z}+\delta_{1z}s)\int_0^L \bar{\beta}N_i\,(\eta+r_i)\left(\frac{\partial N_j}{\partial\eta}+\frac{N_j}{\eta+r_i}\right) d\eta \tag{42}$$

$$\left[K_{22}^{ij}\right] = \int_0^L \left[(\delta_{2z}+\delta_{1z}s)\left(1+\tau_q s+\frac{\tau_q^2}{2}s^2\right)\frac{\rho cs}{\rho_m c_m}N_jN_i\,(\eta+r_i)+\frac{(1+\tau_v s)}{a_0}K^*\,(\eta+r_i)\frac{\partial N_i}{\partial\eta}\frac{\partial N_j}{\partial\eta} + (\delta_{2z}+\delta_{1z}s)\frac{(1+\tau_T s)}{K_m}K\,(\eta+r_i)\frac{\partial N_i}{\partial\eta}\frac{\partial N_j}{\partial\eta}\right] d\eta \tag{43}$$

$$\left\{F^{(e)}\right\} = \begin{Bmatrix} f_{11} \\ f_{21} \end{Bmatrix} \qquad \left\{Q^{(e)}\right\} = \begin{Bmatrix} q_{11} \\ q_{21} \end{Bmatrix} \tag{44}$$

where $f_{11} = \left(\bar{\lambda} + 2\mu\right)\left[N_i\left(\eta + r_i\right)\frac{\partial \bar{u}^{(e)}}{\partial \eta}\right]\Big|_{\eta=r_i}$, $f_{21} = -\left(\bar{\lambda} + 2\mu\right)\left[N_i\left(\eta + r_i\right)^2\frac{\partial \bar{u}^{(e)}}{\partial \eta}\right]\Big|_{\eta=r_{i+1}}$

$$q_{11} = \frac{(1+\tau_v s)}{a_0}K^*\left[N_i\left(\eta + r_i\right)\frac{\partial \bar{\theta}^{(e)}}{\partial \eta}\right]\Big|_{\eta=r_i} + \left(\delta_{2z} + \delta_{1z}s\right)\frac{(1+\tau_T s)}{K_m}K\left[N_i\left(\eta + r_i\right)\frac{\partial \bar{\theta}^{(e)}}{\partial \eta}\right]\Big|_{\eta=r_i},$$

and

$$q_{21} = -\left\{\frac{(1+\tau_v s)}{a_0}K^*\left[N_i\left(\eta + r_i\right)\frac{\partial \bar{\theta}^{(e)}}{\partial \eta}\right]\Big|_{\eta=r_{i+1}} + \left(\delta_{2z} + \delta_{1z}s\right)\frac{(1+\tau_T s)}{K_m}K\left[N_i\left(\eta + r_i\right)\frac{\partial \bar{\theta}^{(e)}}{\partial \eta}\right]\Big|_{\eta=r_{i+1}}\right\}.$$

The unknown nodal values of displacement and temperature for the base element are given by the sub matrices $\left\{\bar{U}^{(e)}\right\}$, $\left\{\bar{\theta}^{(e)}\right\}$, respectively.

Now, the element matrices given by Eqs. (40)–(43) are generated within a loop to construct the general matrix of Eq. (39), where after the assembly of all elements in the solution domain we can construct a system of linear algebraic equations for the solution of unknown nodal values of displacement and temperature. While assembling, it is noted that the right-hand side terms of Eqs. (37) and (38) cancel each other between any two adjacent elements, except the first node of the first element and the last node of the last element. These are the nodes located on the inside and outside boundaries of the disk and, therefore, may be related to the boundary conditions of the disk given by Eq. (33).

Eq. (33) together with Eq. (29) yield

$$\begin{aligned} &\bar{\theta}_1 = 10000/\left(s^2 + 10000s\right), \qquad -a\left(\bar{\lambda}_c + 2\mu_c\right)\frac{\partial \bar{u}^{(e)}}{\partial \eta}\Big|_1 = \lambda_c \bar{U}_1 - \frac{a\left(\bar{\lambda}_m + 2\mu_m\right)\bar{\beta}_c}{\bar{\beta}_m}\bar{\theta}_1 \\ &\frac{\partial \bar{\theta}^{(e)}}{\partial \eta}\Big|_M = 0, \qquad \bar{U}_M = 0 \end{aligned} \tag{45}$$

where $\bar{U}_1$ and $\bar{U}_M$ are the radial displacements of the inner and outer boundaries of the disk, respectively. Also 1 and M are referred to the first and last nodes of the solution domain that are located at the inner and outer radii of the disk, respectively. Further, in view of (33) we find that

$$\frac{\partial \bar{\theta}^{(e)}}{\partial \eta}\Big|_1 = 0 \quad \text{and} \quad \frac{\partial \bar{u}^{(e)}}{\partial \eta}\Big|_M = 0.$$

Therefore, the global force matrix is obtained as $\begin{Bmatrix} \{F\} \\ \{Q\} \end{Bmatrix}$, where the sub matrices $\{F\}$ and $\{Q\}$ are given by

$$\{F\} = \begin{Bmatrix} \bar{\lambda}_c \bar{U}_1 - \dfrac{a\left(\bar{\lambda}_m + 2\mu_m\right)\bar{\beta}_c}{\bar{\beta}_m}\bar{\theta}_1 \\ 0 \\ \vdots \\ 0 \end{Bmatrix}, \qquad \{Q\} = \begin{Bmatrix} 0 \\ 0 \\ \vdots \\ 0 \end{Bmatrix}. \tag{46}$$

All the unknowns can therefore be obtained by solving the above mentioned system of equations. This will yield the solution for the nodal values of displacement and temperature in the Laplace transform domain. For the inversion of Laplace transform, we can finally employ the numerical method of Laplace inversion introduced by Bellman et al. [38]. The method is outlined in the Appendix. This will provide the final solution of the problem in space–time domain.

6. Numerical results and discussion

Now, we develop an efficient computer program using Mathematica to solve the problem numerically as mentioned in the Section 5. We make an attempt to analyze the effects of time, non-homogeneity index and phase-lag parameters on the distributions of displacement, temperature and stresses inside the hollow disk which is considered to be initially at reference temperature $T_0 = 298$ K and subjected to the boundary conditions (28). For the metal and ceramic constituents of the functionally graded disk, titanium and zirconia are considered. Therefore, the inner and outer surfaces of the disk are made of titanium and zirconia, whose properties are taken in SI units as follows [25]:

For titanium:

$$\begin{aligned} &E_m = 66.2\ \text{GPa}, \qquad \nu = 0.321, \qquad \alpha_m = 10.3 \times 10^{-6}\ \text{K}^{-1}, \\ &c_m = 808.3\ \text{J kg}^{-1}\ \text{K}^{-1}, \qquad \rho_m = 4410\ \text{kg m}^{-3}, \qquad K_m = 18.1\ (\text{K s})^{-1}. \end{aligned}$$

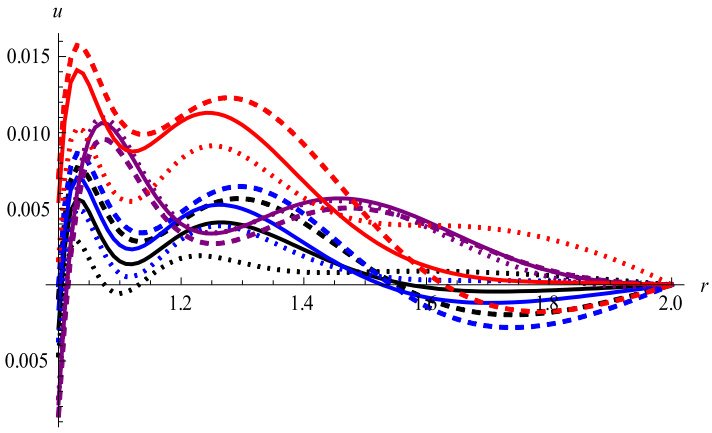

Fig. 2a. Displacement distribution at time $t = 0.026$. (Dashed line: $n = 1$; Solid line: $n = 2$; Dotted line: $n = 3$; Purple color: GN-III; Black Color: ETE; Blue Color: DPLTE; Red color: TPLTE). (For interpretation of the references to colour in this figure legend, the reader is referred to the web version of this article.)

For zirconia:

$$E_c = 117.0\ \text{GPa}, \qquad \nu = 0.333 \qquad \alpha_c = 7.11 \times 10^{-6}\ \text{K}^{-1},$$
$$c_c = 615.6\ \text{J kg}^{-1}\ \text{K}^{-1}, \qquad \rho_c = 5600\ \text{kg m}^{-3}, \qquad K_c = 2.036\ (\text{K s})^{-1}.$$

The dimensionless values of 'a' and 'b', i.e., the inner and outer radii of the disk are taken to be 1 and 2, respectively. The phase-lag parameters are taken as $\tau_v = 0.2$, $\tau_T = 0.5$ and $\tau_q = 0.7$. The rate of thermal conductivity is taken as $K^* = c\,(\lambda + 2\mu)\,/4$ [34]. Although the presented formulation is general, but for computational work, the linear Lagrangian polynomials are used as shape functions in the base element and the geometry of the hollow disk is divided into 100 elements along the radial direction. We computed the values of the desired field variables like, displacement, temperature and stresses in the physical domain inside the disk at different times with different non-homogeneity index n for various thermoelastic theories. Dashed lines, solid lines and dotted lines represent the plots for $n = 1$, $n = 2$ and $n = 3$, respectively. Purple color, black color, blue color and red color indicate the plots for GN-III, ETE, DPLTE and TPLTE, respectively. The solutions displayed in different figures are clearly in agreement with the boundary conditions.

Figs. 2–5 show the variation of displacement, temperature, radial stress and hoop stress along the radial distance 'r' of the disk at different times with different non-homogeneity index 'n' in the contexts of various thermoelasticity theories. Figs. 2a and 2b display the displacement distribution at times $t = 0.026$ and $t = 0.35$, respectively. The temperature distribution at times $t = 0.026$ and $t = 0.35$ are plotted in Figs. 3a and 3b, respectively. In a similar manner the graphs of radial and hoop stress at time $t = 0.026$ are plotted in Figs. 4a and 5a and at time $t = 0.35$ are plotted in Figs. 4b and 5b, respectively. It is clear from these Figures that ETE and DPLTE predict a similar pattern of behavior, however DPLTE predict bit larger numerical values and high amplitudes as compared to ETE for all the profiles. This effect is significant upon displacement and radial stress at all times but at higher times it is also prominent for temperature and hoop stress. When we compare the theories having phase-lags (i.e., DPLTE and TPLTE) with ETE, we observe that the qualitative nature of these three theories are nearly similar at initial time however with the passage of time TPLTE predicts significantly high numerical values and amplitudes for all the fields as compared to two other models. Due to the absence of phase-lags and presence of K^*, GN-III predicts quite different nature specially in the cases of temperature and hoop stress. GN-III shows larger effective region as compared to other three models for all the profiles. At lower times the effect of thermal exposure is visible near the inner surface of disk but as time passes this effect covers more area of disk and also visible towards the outer surface of disk which means the region of influence increases with the increase of time i.e. all the fields vanish at a later distance from the inner surface of the disk when time is increased.

The effect of non-homogeneity index 'n' is most significant upon TPLTE and it decreases in an order as DPLTE, ETE and GN-III i.e. the effect of n is least under GN-III theory. It is noted that as n increases the effective region is decreased and also as n increases the difference between the thermoelasticity theories with phase-lags increases inside the disk. It is evident from Figs. 2–5 that under all four theories although at lower time the effect of 'n' is not significant on temperature and hoop stress but as time passes the effect of 'n' becomes significant on all the profiles. The effect of non-homogeneity index is observed to be the most on the radial stress. Furthermore, it is revealed that in the effected region, the amplitudes of displacement, temperature and stress waves increase with the increase of the non-homogeneity index, n.

Figs. 6–9 display the distributions of displacement, temperature, radial stress and hoop stress with variation of time at the middle of the disk for different values of power law index in the contexts of various thermoelasticity theories. The nature of variation of the fields clearly changes with time and a prominent effect of time upon all profiles under all the theories is indicated. It may be seen from these figures that at the initial time of interaction, i.e. at lower times TPLTE, DPLTE and ETE follow almost a qualitatively similar variations but as time increases the amplitude of oscillations of displacement,

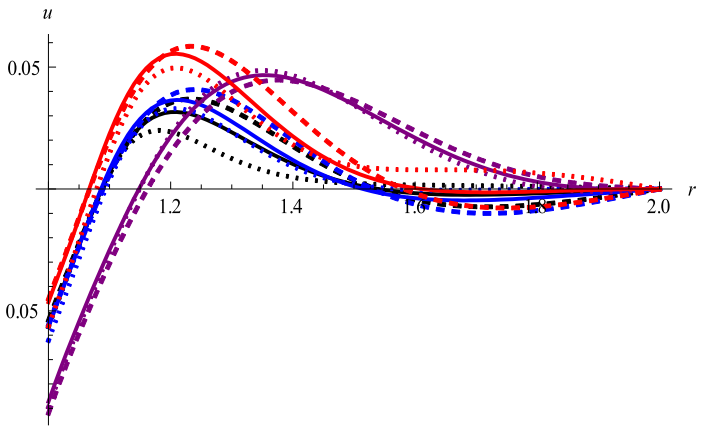

Fig. 2b. Displacement distribution at time $t = 0.35$. (Dashed line: $n = 1$; Solid line: $n = 2$; Dotted line: $n = 3$; Purple color: GN-III; Black Color: ETE; Blue Color: DPLTE; Red color: TPLTE). (For interpretation of the references to colour in this figure legend, the reader is referred to the web version of this article.)

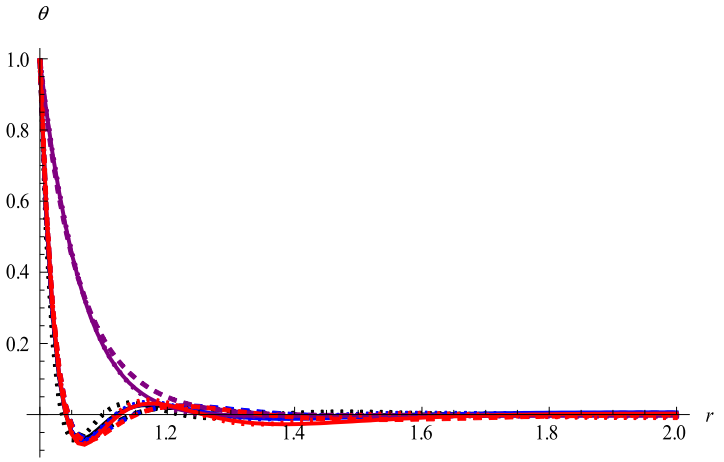

Fig. 3a. Temperature distribution at time $t = 0.026$. (Dashed line: $n = 1$; Solid line: $n = 2$; Dotted line: $n = 3$; Purple color: GN-III; Black Color: ETE; Blue Color: DPLTE; Red color: TPLTE). (For interpretation of the references to colour in this figure legend, the reader is referred to the web version of this article.)

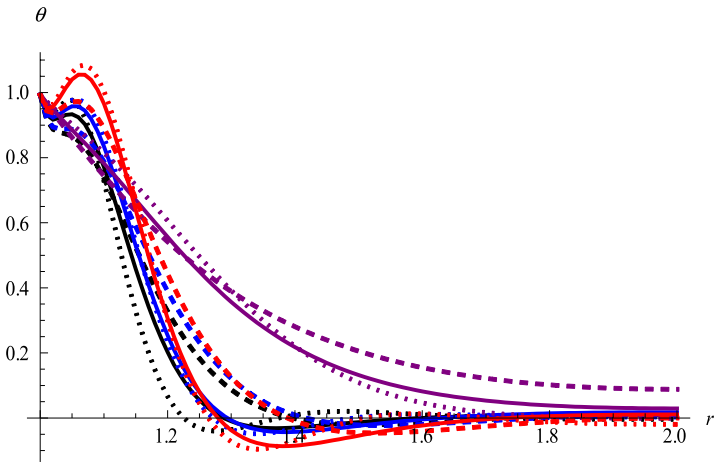

Fig. 3b. Temperature distribution at time $t = 0.35$. (Dashed line: $n = 1$; Solid line: $n = 2$; Dotted line: $n = 3$; Purple color: GN-III; Black Color: ETE; Blue Color: DPLTE; Red color: TPLTE). (For interpretation of the references to colour in this figure legend, the reader is referred to the web version of this article.)

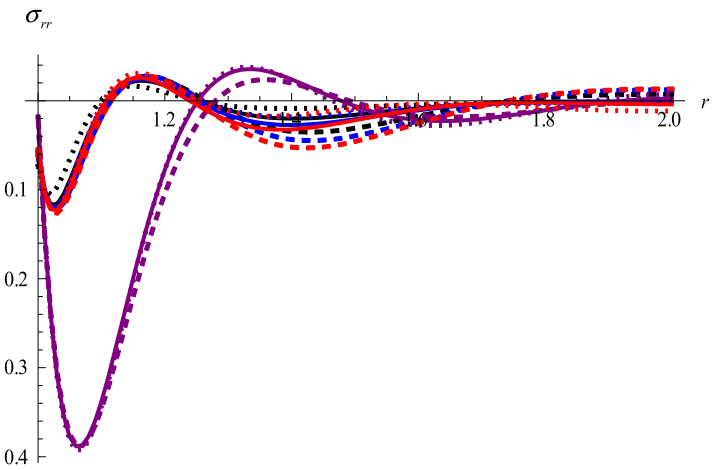

Fig. 4a. Radial stress distribution at time $t = 0.026$. (Dashed line: $n = 1$; Solid line: $n = 2$; Dotted line: $n = 3$; Purple color: GN-III; Black Color: ETE; Blue Color: DPLTE; Red color: TPLTE). (For interpretation of the references to colour in this figure legend, the reader is referred to the web version of this article.)

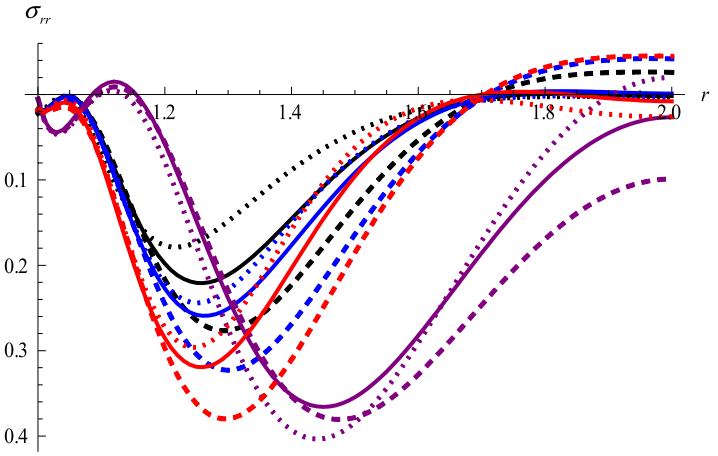

Fig. 4b. Radial stress distribution at time $t = 0.35$. (Dashed line: $n = 1$; Solid line: $n = 2$; Dotted line: $n = 3$; Purple color: GN-III; Black Color: ETE; Blue Color: DPLTE; Red color: TPLTE). (For interpretation of the references to colour in this figure legend, the reader is referred to the web version of this article.)

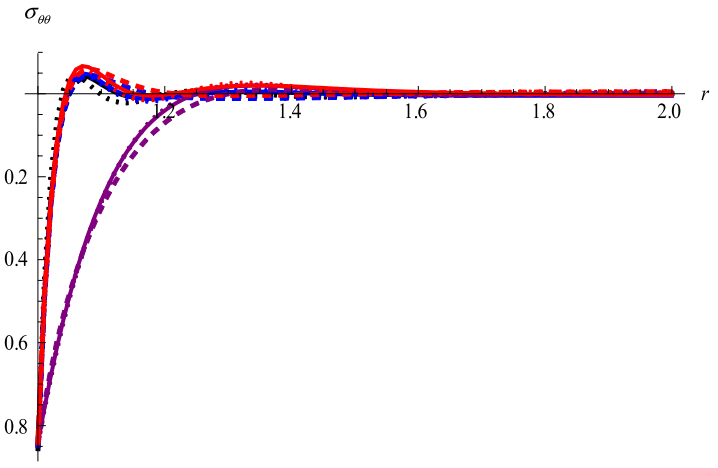

Fig. 5a. Hoop stress distribution at time $t = 0.026$. (Dashed line: $n = 1$; Solid line: $n = 2$; Dotted line: $n = 3$; Purple color: GN-III; Black Color: ETE; Blue Color: DPLTE; Red color: TPLTE). (For interpretation of the references to colour in this figure legend, the reader is referred to the web version of this article.)

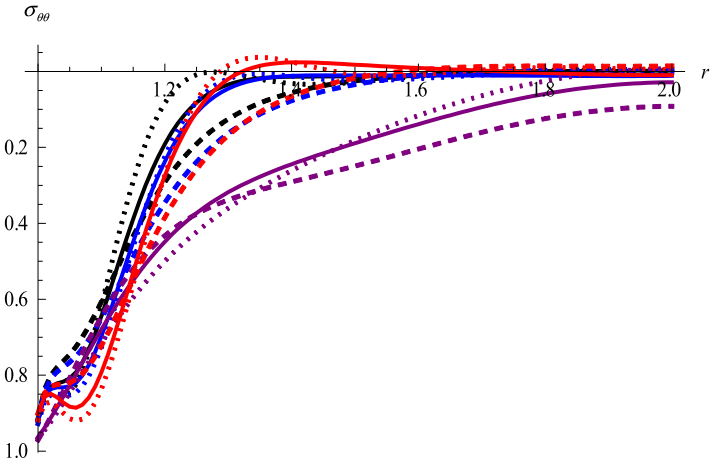

Fig. 5b. Hoop stress distribution at time $t = 0.35$. (Dashed line: $n = 1$; Solid line: $n = 2$; Dotted line: $n = 3$; Purple color: GN-III; Black Color: ETE; Blue Color: DPLTE; Red color: TPLTE). (For interpretation of the references to colour in this figure legend, the reader is referred to the web version of this article.)

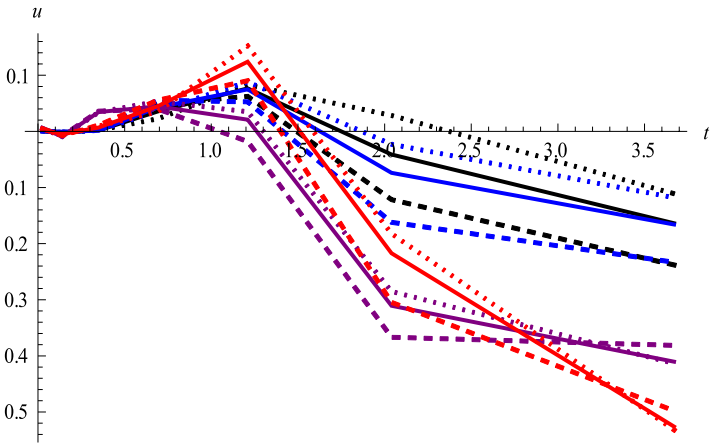

Fig. 6. Time variation of displacement at middle of the disk. (Dashed line: $n = 1$; Solid line: $n = 2$; Dotted line: $n = 3$; Purple color: GN-III; Black Color: ETE; Blue Color: DPLTE; Red color: TPLTE). (For interpretation of the references to colour in this figure legend, the reader is referred to the web version of this article.)

temperature and stresses increase significantly under TPLTE as compared to DPLTE and ETE. However, a distinctly different behavior is observed in the case of GN-III model as compared to other three models. The maximum of displacement, temperature, radial stress and hoop stress variations reduce when n is increased. Also the amplitude of oscillations of these waves is reduced when n has larger values. This effect is more prominent upon TPLTE, DPLTE and ETE as compared to GN-III. Thus when a thermal shock is applied to the boundary of the disk, functionally graded disk may be used as thermal barrier to reduce the thermal shock effects and thermoelasticity theories with phase-lags may be employed as compared to GN-III model in this respect.

7. Validity of formulation

To verify the present formulation and numerical results, we need to compare the results between the present work and known data in the literature. For this purpose, we establish a comparison through Fig. 10 between the results of the present work and the results of [27] by considering the same boundary conditions as given in [27] and for the same functionally graded material with non-homogeneity index considered as $n = 1$. We observe a similar pattern between the results which verifies the present formulation to be correct.

8. Conclusions

We study a problem of functionally graded annular disk of thermoelastic medium in the context of four thermoelasticity theories namely, GN-III, ETE, DPLTE and TPLTE by considering a unified coupled heat conduction equation. The solution of

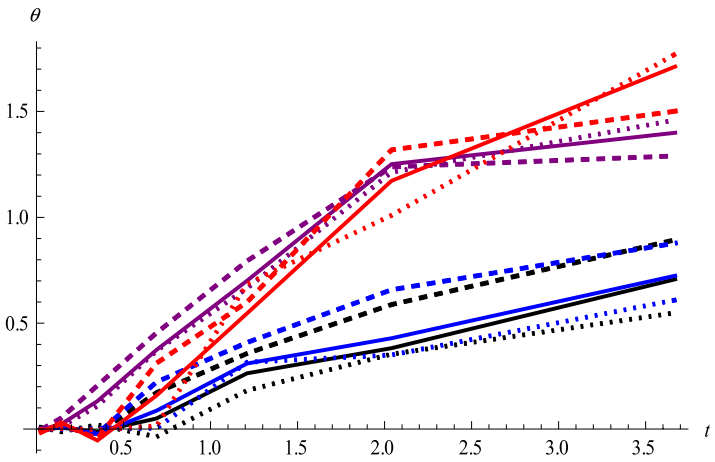

Fig. 7. Time variation of temperature at middle of the disk. (Dashed line: $n = 1$; Solid line: $n = 2$; Dotted line: $n = 3$; Purple color: GN-III; Black Color: ETE; Blue Color: DPLTE; Red color: TPLTE). (For interpretation of the references to colour in this figure legend, the reader is referred to the web version of this article.)

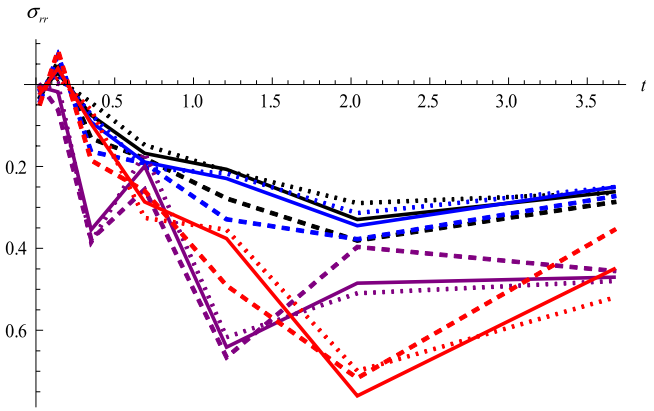

Fig. 8. Time variation of radial stress at middle of the disk. (Dashed line: $n = 1$; Solid line: $n = 2$; Dotted line: $n = 3$; Purple color: GN-III; Black Color: ETE; Blue Color: DPLTE; Red color: TPLTE). (For interpretation of the references to colour in this figure legend, the reader is referred to the web version of this article.)

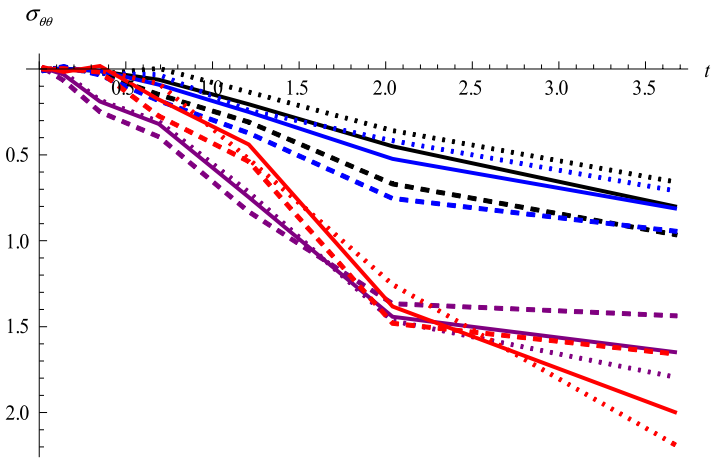

Fig. 9. Time variation of hoop stress at middle of the disk. (Dashed line: $n = 1$; Solid line: $n = 2$; Dotted line: $n = 3$; Purple color: GN-III; Black Color: ETE; Blue Color: DPLTE; Red color: TPLTE). (For interpretation of the references to colour in this figure legend, the reader is referred to the web version of this article.)

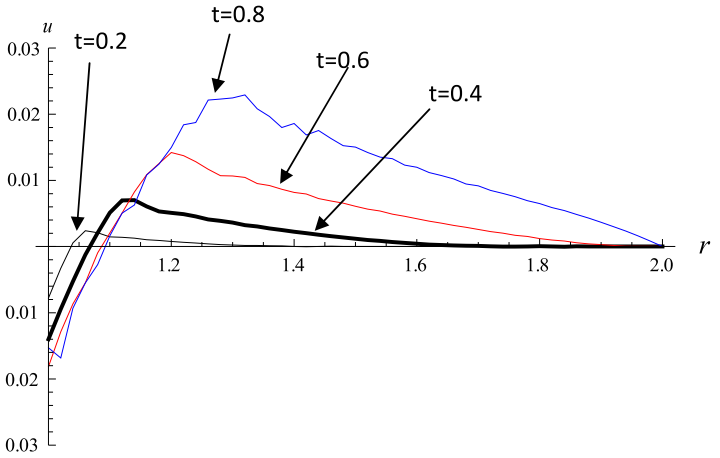

Fig. 10. Displacement distribution at four different times for same functionally graded material ($n = 1$) with similar boundary conditions as in [27].

coupled field equations for displacement and temperature is obtained by using Galerkin finite element method. Distribution of displacement, temperature, radial stress and hoop stress are plotted along the radius at different times. The time variations of all profiles at middle of the hollow disk are also shown. The effects of phase-lags, non-homogeneity index and time are investigated through the figures. It is observed that among the theories involving phase-lags, at lower time qualitative behavior of these theories are similar although at higher times GN-III and TPLTE predict significantly high numerical values and amplitudes for all the profiles as compared to two other models. GN-III shows larger effective region as compared to TPLTE, DPLTE and ETE for all the profiles. It is seen that when n increases the amplitude of oscillations of displacement, temperature, radial stress and hoop stress variations reduce.

Acknowledgment

We are thankful to the reviewers for their constructive suggestions to improve the quality of our paper.

Appendix. Numerical method for inversion of Laplace transforms (Bellman et al. [38])

Let the Laplace transform of a function $u(t)$ be defined by

$$\bar{F}(p) = \int_0^\infty u(t)e^{-pt}dt, \quad p > 0. \tag{A.1}$$

We assume that $u(t)$ is sufficiently smooth to permit the approximate method we apply [38]. Putting $x = e^{-t}$ in Eq. (A.1) we obtain

$$\bar{F}(p) = \int_0^1 x^{p-1}G(x)dx, \tag{A.2}$$

where $G(x) = u(-\ln(x))$.

Applying the Gaussian quadrature formula to Eq. (A.2) yields

$$\sum_{i-1}^{N} W_i x_i^{p-1} G(x_i) = \bar{F}(p) \tag{A.3}$$

where x_i $(i = 1, 2, 3, \ldots, N)$ are the roots of the shifted Legendre polynomial $P_N(x) = 0$ and W_i $(i = 1, 2, 3, \ldots, N)$ are the corresponding weights.

Eq. (A.3) can be written as

$$W_1 x_1^{p-1}G(x_1) + W_2 x_2^{p-1}G(x_2) + W_3 x_3^{p-1}G(x_3) + \cdots + W_N x_N^{p-1}G(x_N) = \bar{F}(p). \tag{A.4}$$

Now, we put $p = 1, 2, \ldots, N$ in Eq. (A.4) and obtain the following system of equations

$$\begin{aligned}
&W_1G(x_1) + W_2G(x_2) + W_3G(x_3) + \cdots + W_NG(x_N) = \bar{F}(1)\\
&W_1x_1G(x_1) + W_2x_2G(x_2) + W_3x_3G(x_3) + \cdots + W_Nx_NG(x_N) = \bar{F}(2)\\
&\ldots\\
&W_1x_1^{N-1}G(x_1) + W_2x_2^{N-1}G(x_2) + W_3x_3^{N-1}G(x_3) + \cdots + W_Nx_N^{N-1}G(x_N) = \bar{F}(N).
\end{aligned} \tag{A.5}$$

Therefore, from Eq. (A.5) we obtain $G(x_i)$ in the form

$$\begin{bmatrix} G(x_1) \\ G(x_2) \\ \dots \\ G(x_N) \end{bmatrix} = \begin{bmatrix} W_1 & W_2 & \dots & W_N \\ W_1x_1 & W_2x_2 & \dots & W_Nx_N \\ \dots & \dots & \dots & \dots \\ W_1x_1^{N-1} & W_2x_2^{N-1} & \dots & W_Nx_N^{N-1} \end{bmatrix}^{-1} \begin{bmatrix} \bar{F}(1) \\ \bar{F}(2) \\ \dots \\ \bar{F}(N) \end{bmatrix}. \tag{A.6}$$

For $N = 7$, we have the following set of values for x_i and W_i:

The roots of the shifted Legendre polynomial	Corresponding weights (W_i)
$x_1 = 0.02555604382862$	0.06474248308443
$x_2 = 0.12923440720030$	0.13985269574463
$x_3 = 0.29707742431130$	0.19091502525255
$x_4 = 0.500000000000000$	0.20897959183673
$x_5 = 0.702922575688698$	0.190915025252559
$x_6 = 0.870765592799697$	0.139852695744638
$x_7 = 0.974553956171379$	0.064742483084435

From Eq. (A.6) we can calculate the discrete values of $G(x_i)$, i.e., $u(t_i)$ where $t_i = -\ln(x_i) = 3.67119, 2.04612, 1.21376, 0.693147, 0.352509, 0.138382, 0.0257750$. Finally using interpolation, we obtain the function $u(t)$.

References

[1] M.A. Biot, Thermoelasticity and irreversible thermodynamics, J. Appl. Phys. 27 (1956) 240–253.
[2] H.W. Lord, Y. Shulman, A generalized dynamical theory of thermoelasticity, J. Mech. Phys. Solids 15 (1967) 299–309.
[3] A.E. Green, K.A. Lindsay, Thermoelasticity, J. Elasticity 2 (1972) 1–7.
[4] A.E. Green, P.M. Naghdi, A re-examination of the basic postulates of thermomechanics, Proc. R. Soc. Lond. Ser. A 432 (1991) 171–194.
[5] A.E. Green, P.M. Naghdi, On undamped heat waves in an elastic solid, J. Therm. Stresses 15 (1992) 253–264.
[6] A.E. Green, P.M. Naghdi, Thermoelasticity without energy dissipation, J. Elasticity 311 (1993) 89–209.
[7] M.N. Ozisik, D.Y. Tzou, On the wave theory of heat conduction, J. Heat Transf. (ASME) 116 (1994) 526–535.
[8] D.Y. Tzou, A unified field approach for heat conduction from macro to micro scales, J. Heat Transfer (ASME) 117 (1995) 8–16.
[9] D.S. Chandrasekharaiah, Hyperbolic thermoelasticity: A review of recent literature, Appl. Mech. Rev. 51 (1998) 705–729.
[10] S.K. Roychoudhuri, On a thermoelastic three phase-lag model, J. Therm. Stresses 30 (2007) 231–238.
[11] V. Birman, L.W. Byrd, Modeling and analysis of functionally graded materials and structures, Appl. Mech. Rev. 60 (2007) 195–216.
[12] A. Bagri, M.R. Eslami, Analysis of thermoelastic waves in functionally graded hollow spheres based on the Green–Lindsay theory, J. Therm. Stresses 30 (2007) 1175–1193.
[13] Y. Tanigawa, Some basic thermoelastic problems for non-homogeneous structural materials, Appl. Mech. Rev. 48 (6) (1995) 287–300.
[14] Y. Obata, Noda, Steady Thermal stresses in a hollow circular cylinder and a hollow sphere of functionally gradient material, J. Therm. Stresses 17 (1994) 471–488.
[15] M.P. Lutz, R.W. Zimmerman, Thermal stresses and effective thermal expansion coefficient of a functionally graded sphere, J. Therm. Stresses 19 (1996) 39–54.
[16] R.W. Zimmerman, M.P. Lutz, Thermal stress and effective thermal expansion in a uniformly heated functionally graded cylinder, J. Therm. Stresses 22 (1999) 177–188.
[17] J.N. Reddy, C.D. Chin, Thermomechanical analysis of functionally graded cylinders and plates, J. Therm. Stresses 21 (1998) 593–626.
[18] S.P. Jeon, Y. Tanigawa, D. Sone, Analytical treatment of axisymmetric thermoelastic field with Kassir's nonhomogeneous material properties and its adaptation to boundary value problem of slab under steady temperature field, J. Therm. Stresses 20 (1997) 325–343.
[19] S.S. Vel, R.C. Betra, Exact solution of thermoelastic deformations of functionally graded thick rectangular plates, AIAA J. 40 (2002) 1421–1433.
[20] L.F. Qian, R.C. Betra, Transient thermoelastic deformations of a thick functionally graded plate, J. Therm. Stresses 27 (2004) 705–740.
[21] G.R. Ye, W.Q. Chen, G.B. Cai, A uniformly heated functionally graded cylindrical shell with transverse isotropy, Mech. Res. Commun. 28 (2001) 535–542.
[22] A.M. El-Naggar, A.M. Abd-Alla, M.A. Fahmy, S.M. Ahmed, Thermal stresses in a rotating non-homogeneous orthotropic hollow cylinder, Heat Mass Transfer 39 (2002) 41–46.
[23] M.R. Eslami, M.H. Babai, R. Poultangari, Thermal and mechanical stresses in a functionally graded thick sphere, Int. J. Press. Vessels Pip. 82 (2005) 522–527.
[24] M. Bakhshi, A. Bagri, M.R. Eslami, Coupled thermoelasticity of functionally graded disk, Mech. Adv. Mater. Struc. 13 (3) (2006) 219–225.
[25] A. Bahtui, M.R. Eslami, Coupled thermoelasticity of functionally graded cylindrical shells, Mech. Res. Commun. 34 (1) (2007) 1–18.
[26] A. Bahtui, M.R. Eslami, Generalized coupled thermoelasticity of functionally graded cylindrical shells, Int. J. Numer. Methods Eng. 69 (2007) 676–697.
[27] A. Bagri, M.R. Eslami, Generalized coupled thermoelasticity of functionally graded annular disk considering the Lord–Shulman theory, Compos. Struct. 83 (2008) 168–179.
[28] E. Carrera, S. Brischetto, M. Cinefra, M. Soave, Effects of thickness stretching in functionally graded plates and shells, Composites: Part B 42 (2011) 123–133.
[29] M.E. Golmakani, M. Kadkhodayan, Large deflection analysis of circular and annular FGM plates under thermo-mechanical loadings with temperature-dependent properties, Composites: Part B 42 (2011) 614–625.
[30] D. Sun, Song-Nan Luo, Wave propagation and transient response of functionally graded material circular plates under a point impact load, Composites: Part B 42 (2011) 657–665.
[31] M.A. Ezzat, H.M. Atef, Magneto-electro viscoelastic layer in functionally graded materials, Composites: Part B 42 (2011) 832–841.
[32] M.K. Ghosh, M. Kanoria, Generalized thermoelastic functionally graded spherically isotropic solid containing a spherical cavity under thermal shock, Appl. Math. Mech. 29 (10) (2008) 1263–1278.
[33] M.K. Ghosh, M. Kanoria, Analysis of thermoelastic response in a functionally graded spherically isotropic hollow sphere based on Green–Lindsay theory, Acta Mech. 207 (2009) 51–67.
[34] S.H. Mallik, M. Kanoria, Generalized thermoelastic functionally graded solid with a periodically varying heat source, Int. J. Solids Struct. 44 (2007) 7633–7645.
[35] S. Banik, M. Kanoria, Generalized thermoelastic interaction in a functionally graded isotropic unbounded medium due to varying heat source with three-phase-lag effect, Math. Mech. Solids (2012) http://dx.doi.org/10.1177/1081286511436191.

[36] S.M. Hosseini, Coupled thermoelasticity and second sound in finite length functionally graded thick hollow cylinders (without energy dissipation), Mater. Des. 30 (2009) 2011–2023.
[37] R.B. Hetnarski, M.R. Eslami, in: G.M.L. Gladwell (Ed.), Thermal Stresses: Advanced Theory and Applications, in: Solid Mechanics and its Applications, vol. 158, Springer, 2010.
[38] R. Bellman, R.E. Kolaba, J.A. Lockette, Numerical Inversion of the Laplace Transform, American Elsevier Publishing Company, New York, 1966.